

# Disc distortion revisited

James Binney<sup>1\*</sup>

<sup>1</sup>*Rudolf Peierls Centre for Theoretical Physics, Clarendon Laboratory, Parks Road, Oxford, OX1 3PU, UK*

8 November 2024

## ABSTRACT

We revisit the dynamics of razor-thin, stone-cold, self-gravitating discs. By recasting the equations into standard cylindrical coordinates, the linearised vertical dynamics of an exponential disc can be followed for several gigayears on a laptop in a few minutes. An initially warped disc rapidly evolves into a flat inner region and an outward-propagating spiral corrugation wave that rapidly winds up and would quickly thicken a disc with non-zero radial velocity dispersion. The Sgr dwarf galaxy generates a similar warp in the Galactic disc as it passes through pericentre, and the warp generated by the dwarf’s last pericentre  $\sim 35$  Myr ago is remarkably similar to the warp traced by the Galaxy’s HI disc. The resemblance to the observed warp is fleeting but its timing is perfect. For the adopted parameters the amplitude of the model warp is a factor 3 too small, but there are several reasons for this being so. The marked flaring of our Galaxy’s low- $\alpha$  disc just outside the solar circle can be explained as a legacy of earlier pericentres.

**Key words:** Galaxy: kinematics and dynamics – galaxies: kinematics and dynamics – methods: numerical

## 1 INTRODUCTION

The discs of spiral galaxies are typically remarkably planar inside three disc scale-lengths  $R_d$  but frequently become warped further out. Early observations at 21 cm revealed this structure in the case of the Milky Way (Burke 1957; Kerr 1957), and 21-cm observations with the Westerbork Aperture Synthesis Radio Telescope revealed similar structure in a significant fraction of nearby spiral galaxies (Bosma 1978). Briggs (1990) summarised and systematised the phenomenology of the galactic warps.

Data regarding the planarity of stellar discs are much less abundant for several reasons. One issue is that a galaxy’s stellar disc is much thicker than its HI disc, so small deviations from planarity can be hidden in the disc’s thickness. Moreover, the mean velocity of a stellar disc is much harder to measure with precision than the mean velocity of the HI disc, so the velocities associated with warps are harder to detect in the stellar disc. These issues are least acute in the case of the Milky Way, but historically the interpretation of data for the Milky Way has been made uncertain by uncertain distances to stars. With the advent of the third data release by ESA’s Gaia mission (Gaia Collaboration et al. 2023) our ability to probe the vertical dynamics of the Milky Way has dramatically improved. This turn of events calls for a corresponding improvement in the dynamical theory of warped discs.

The standard path to deep understanding in physics is usually linear theory. Given that the most massive parts of galactic discs are planar to a very good approximation, we naturally seek a linear theory of discs’ vertical perturbations. The problem cannot be approached by direct analogy with spiral structure, that is by linearising the stellar disc’s distribution function  $f(\mathbf{x}, \mathbf{v})$ , because the disc is thin, so the unperturbed distribution function (DF),  $f_0$ , changes by order of itself when the vertical coordinate  $z$  changes by the disc’s scale height, which is comparable to the amplitude of even a small warp.

Since the problem is not accessible to Eulerian perturbation theory, Hunter & Toomre 1969, (hereafter HT69) developed a linearised Lagrangian theory of vertical disturbances of a razor-thin disc by modelling the unperturbed disc as a system of  $N$  perfectly circular, co-planar orbits and allowing orbits to develop small inclinations. With  $h(R)$  denoting the amplitude of the vertical excursions of orbits at radius  $R$ , they derived  $2N$  equations of motion linear in the small parameter  $h/R$ . They investigated the normal modes of this system, hoping to find discrete normal modes that resembled observed warps. They concluded, however, that the system’s spectrum tends to a continuum as  $N \rightarrow \infty$  whenever the disc has a realistically smooth decline in density at large radii.

When a system’s spectrum forms a continuum, perturbations of the system will always be spread among modes that cover a non-negligible range of frequencies, with the consequence that the perturbation will fade away as the

\* E-mail: binney@thphys.ox.ac.uk

phases of individual modes drift towards a random distribution. Since the pioneering work of HT69 we have recognised that all stellar systems have continuous spectra and that this fact underpins the dissipative nature of their dynamics that is familiar from N-body simulations (e.g. Lau & Binney 2021).

Given the continuous nature of the spectra established by HT69 straightforward integration of the equations of motion offers a more profitable route to understanding disc dynamics than normal-mode analysis. HT69 performed some integrations, but they examined only an infinitesimal fraction of the interesting possibilities, for two main reasons: (i) their equations related to a coordinate system that is not well suited to exponential discs, and (ii) they did not include a dark halo because they were writing before dark haloes became accepted features of galactic structure.

When dark haloes had become established, the normal-mode approach to disc dynamics was revived in the expectation that a flattened dark halo would permit the existence of a non-trivial and isolated ‘tilt’ mode that might explain observed warps (Toomre 1983; Sparke & Casertano 1988). An isolated tilt mode can be found if the dark halo’s potential is assumed to be fixed, but when the back-reaction of a perturbed dark halo is included in the disc’s dynamics, the tilt mode dissolves and warps phase-mix away as they do in an isolated disc (Nelson & Tremaine 1995; Binney et al. 1998).

The practical impossibility of long-lived warp configurations leads one to investigate the evolution of warps in the time rather than the frequency domain. Here we return to the approach pioneered by HT69 and too rarely employed since. Instead of using the oblate-spheroidal coordinate system that HT69 used, we show that the dynamical equations can be integrated cheaply in standard cylindrical polar coordinates when advantage is taken of the Greens function for Poisson’s equation that was introduced by Cohl & Tohline (1999). The problem’s equations are derived in Section 2 – they differ slightly from those derived in HT69 as is discussed in Appendices A and B. In Section 3 we investigate the evolution of a disc that starts with a simple warp. In Section 4 we explore the effect that the Sgr dwarf galaxy has had on the vertical structure of our Galaxy’s disc. Section 5 discusses the successes, failures and limitations of the HT69 approach to vertical disc dynamics. Section 6 sums up and looks to the future.

## 2 THE EQUATIONS

In this section we obtain the equations that govern the vertical dynamics of particles that move on near-circular orbits under their mutual gravitational attraction.

By solving Laplace’s equation by separation of variables in cylindrical polar coordinates, it can be shown that (Cohl & Tohline 1999)

$$\frac{1}{|\mathbf{x} - \mathbf{x}'|} = \frac{1}{\pi\sqrt{RR'}} \sum_{m=-\infty}^{\infty} Q_{|m|-1/2}(\chi) e^{im(\phi-\phi')}, \quad (1)$$

where  $Q$  is a Legendre function of the second kind and

$$\chi(R, z, R', z') \equiv \frac{R^2 + R'^2 + (z - z')^2}{2RR'}. \quad (2)$$

We apply this expansion to the density distribution

$$\rho(R', \phi', z') = \Sigma(R') \delta(z' - h') \quad (3)$$

of a warped disc, where  $\Sigma(R')$  is the unperturbed surface density and  $h'(R', \phi')$  is the vertical displacement of the disc at  $\mathbf{x}' = (R', \phi')$ . Executing the integral over  $z'$  yields

$$\begin{aligned} \Phi(\mathbf{x}) &= -G \int d^2\mathbf{x}' \Sigma(\mathbf{x}') \frac{\delta(z' - h')}{|\mathbf{x} - \mathbf{x}'|} \\ &= -\frac{G}{\pi} \sum_m \int dR' \sqrt{\frac{R'}{R}} \Sigma(R') \int d\phi' e^{im(\phi-\phi')} Q_{|m|-1/2} \Big|_{z'=h'} \end{aligned} \quad (4)$$

The vertical acceleration generated by  $\Phi$  at  $\mathbf{x} = (R, \phi, h)$  is

$$\begin{aligned} a_z(R, h) &= -\frac{\partial\Phi}{\partial z} \Big|_{z=h} = \frac{G}{\pi} \sum_m \int dR' \sqrt{\frac{R'}{R}} \Sigma(R') \\ &\quad \times \int d\phi' e^{im(\phi-\phi')} \frac{dQ_{|m|-1/2}}{d\chi} \frac{h-h'}{RR'}. \end{aligned} \quad (5)$$

We are seeking an expression for  $a_z$  that’s linear in  $(h - h')/\sqrt{RR'}$ , so we can neglect the dependence of  $dQ/d\chi$  on the small quantity  $(h - h')/\sqrt{RR'}$  by evaluating  $\chi$  with  $z - z' = \epsilon_z$ , a distance that’s much smaller than  $\sqrt{RR'}$  that will be discussed below. This done,  $dQ/d\chi$  becomes independent of  $\phi'$  and can be taken out of the  $\phi'$  integral along with  $e^{im\phi}/RR'$ . We are left with the integral

$$\int d\phi' e^{-im\phi'} (h - h'). \quad (6)$$

The part involving  $h$  vanishes unless  $m = 0$ , when it yields  $2\pi h(R, \phi)$ , while that involving  $h'$  yields  $2\pi h_m(R')$ , where

$$h_m(R) = \int_0^{2\pi} \frac{d\phi}{2\pi} e^{-im\phi} h(R, \phi). \quad (7)$$

Thus

$$\begin{aligned} a_z(R, h) &= \frac{2G}{R^{3/2}} \int \frac{dR'}{\sqrt{R'}} \Sigma(R') \\ &\quad \times \left( \frac{dQ_{-1/2}}{d\chi} h(R, \phi) - \sum_m \frac{dQ_{|m|-1/2}}{d\chi} h_m(R') e^{im\phi} \right). \end{aligned} \quad (8)$$

Multiplying by  $e^{-im\phi}/2\pi$  and integrating over  $\phi$  we obtain an expression for the Fourier coefficients of  $a_z$

$$\begin{aligned} a_{zm} &= \frac{2G}{R^{3/2}} \int \frac{dR'}{\sqrt{R'}} \Sigma(R') \\ &\quad \times \left( \frac{dQ_{-1/2}}{d\chi} h_m(R) - \frac{dQ_{|m|-1/2}}{d\chi} h_m(R') \right). \end{aligned} \quad (9)$$

As  $R' \rightarrow R$ ,  $\chi$  tends to  $1 + \frac{1}{2}(\epsilon_z/R)^2$  and the derivatives of  $Q$  diverge like  $(R/\epsilon_z)^2$ . Nonetheless,  $a_{zm}$  is finite because the divergent parts of the terms proportional to  $h_m(R)$  and  $h_m(R')$  cancel. We avoid singular integrands by subtracting  $(dQ_{|m|-1/2}/d\chi)h_m$  from the first term in the big bracket and adding it to the second term. Then we can write

$$\begin{aligned} a_{zm} &= N_m(R) h_m(R) \\ &\quad - \int \frac{dR'}{\sqrt{R'}} M_m(R, R') [h_m(R') - h_m(R)], \end{aligned} \quad (10)$$

where

$$\begin{aligned} N_m(R) &\equiv \frac{2G}{R^{3/2}} \int \frac{dR'}{\sqrt{R'}} \Sigma(R') \left( \frac{dQ_{-1/2}}{d\chi} - \frac{dQ_{|m|-1/2}}{d\chi} \right) \\ M_m(R, R') &\equiv \frac{2G}{R^{3/2}} \Sigma(R') \frac{dQ_{|m|-1/2}}{d\chi}. \end{aligned} \quad (11)$$

Numerical evaluations show that both contributions to  $a_{zm}$  become independent of  $\epsilon_z$  when the latter is sufficiently small: in the integral for  $N_m$ , the divergencies of the derivatives of  $Q_{-1/2}$  and  $Q_{|m|-1/2}$  cancel, while in the integral over  $M_m$  the factor  $h' - h$  suppresses the contribution from  $R' \simeq R$  in which  $dQ/d\chi$  depends on  $\epsilon_z$ .

We obtain differential equations for  $h_m(R, t)$  from the equation of motion  $\ddot{z} = a_z$  of a star's  $z$  coordinate:  $z$  is the value of  $h$  at the star's location,  $(R, \phi = \phi_0 + \Omega t)$ , where  $\Omega(R)$  is the circular frequency at the star's location. Thus

$$\ddot{z} = \left( \frac{\partial}{\partial t} + \Omega(R) \frac{\partial}{\partial \phi} \right)^2 h = a_z. \quad (12)$$

The Fourier components of  $h$  satisfy corresponding equations

$$\begin{aligned} \ddot{h}_m + 2im\Omega \dot{h}_m - m^2 \Omega^2 h_m &= N_m h_m \\ &- \int \frac{dR'}{\sqrt{R'}} M_m(R, R') [h_m(R') - h_m(R)], \end{aligned} \quad (13)$$

where we have used equation (10) for the acceleration. Each function  $h_m(R)$  satisfies its own p.d.e., completely independent of the other  $h_m$ . Hence in this linear theory we can investigate independently the dynamics of corrugations that are axisymmetric ( $m = 0$ ), or involve tilts ( $m = 1$ ) or have more elaborate angular structure.

From equation (7) it follows that

$$\begin{aligned} z(t) &= h(t, \phi_0 + \Omega t) = h_0 \\ &+ 2 \sum_{m>0} \left( \Re(h_m) \cos[m\phi(t)] - \Im(h_m) \sin[m\phi(t)] \right). \end{aligned} \quad (14)$$

In the important case  $m = 1$ , the line of nodes, in which rings cross the plane  $z = 0$ , lies along

$$\phi = \text{atan2}[\Im(h_1), \Re(h_1)]. \quad (15)$$

Differentiating equation (14) wrt time, we have

$$\begin{aligned} v_z &= 2 \sum_{m>0} [\Re(\dot{h}_m) \cos(m\phi) - \Im(\dot{h}_m) \sin(m\phi)] \\ &- 2 \sum_{m>0} m\Omega [\Re(h_m) \sin(m\phi) + \Im(h_m) \cos(m\phi)]. \end{aligned} \quad (16)$$

The derivation above of the equations of motion (13) is superficially straightforward and simpler than that given by Hunter & Toomre in their classic paper, but it skates over a very delicate point. The issue is explained in Appendix A.

## 2.1 Adding a bulge and dark halo

The gravitational fields of real galaxies include important contributions from spheroidal components such as bulges and dark halos, so we should add the potentials of a bulge and dark halo to the disc's potential. An externally sourced gravitational field modifies equation (13) in two ways. First, it changes  $\Omega(R)$ , which should be the actual circular frequency rather than just the frequency generated by the disc

itself. Second, the external field adds a term  $a_{3z}$  to the right of equation (12) for the vertical acceleration contributed by the external gravitational field. Given that the bulge and halo are reflection-symmetric in the equatorial plane, the potential  $\Phi_e(R, z)$  that they generate must be an even function of  $z$ . Hence its Taylor series gives

$$\Phi_e(R, z) = \Phi_e(R, 0) + \frac{1}{2} \frac{\partial^2 \Phi_e}{\partial z^2} \Big|_{z=0} z^2 + \dots \quad (17)$$

and to a good approximation we have that the corresponding vertical acceleration is  $a_{3z} = -Kz$ , where  $K \equiv \partial^2 \Phi_e / \partial z^2|_{z=0}$  is a positive constant.

It is easy to show that in the case of a spherical external potential  $\Phi_e$  and a corrugation with  $m = 1$ , the additional acceleration  $a_{3z}$  on the right of equation (13) that one gets from equation (17) exactly cancels the increase in  $\Omega^2$  on the left of equation (13)<sup>1</sup>, so the addition of a spherical potential modifies equation (13) only by increasing the magnitude of the Coriolis term  $2im\Omega \dot{h}_m$  that couples the real and imaginary parts of  $h_m$ . The physical consequence of this change is to increase the rate at which rings precess.

## 2.2 Tidal excitation

As many authors have remarked (e.g. McMillan et al. 2022), the Sagittarius dwarf galaxy is probably a major contributor to excitation of the Galactic warp. We can use equations (13) to explore this possibility by adding a suitable tidal forcing to the equations' right sides before integrating them from  $h = \dot{h} = 0$ . We work in the freely-falling frame of the Galactic centre. In this frame the effective gravitational field at  $\mathbf{x}$  due to a perturber with a spherical potential  $\Psi$  is

$$\begin{aligned} \mathbf{g}(t, \mathbf{x}) &= -\nabla \Psi(\mathbf{x} - \mathbf{x}) + \nabla \Psi_{\mathbf{X}} \\ &= \frac{d\Psi}{dr} \Big|_{|\mathbf{x}-\mathbf{x}|} \frac{\mathbf{X} - \mathbf{x}}{|\mathbf{X} - \mathbf{x}|} - \frac{d\Psi}{dr} \Big|_{|\mathbf{x}|} \frac{\mathbf{X}}{|\mathbf{X}|}, \end{aligned} \quad (18)$$

where  $\mathbf{X}(t)$  is the perturber's location relative to the Galactic centre. On a circle of radius  $R$  in the plane, the vertical component of  $\mathbf{g}$  can be Fourier decomposed into the sum

$$\mathbf{e}_z \cdot \mathbf{g}(R, \phi, t) = \sum_m g_m(R, t) e^{im\phi} \quad (19)$$

Vertical excitation of the disc by the dwarf is then obtained by adding  $g_m$  to the right side of equation (13). Unfortunately, the radial and azimuthal excitations have to be ignored.

## 2.3 Integrating the equations of motion

To integrate the equations of motion (13) we introduce a radial grid  $R_n$  by the rule

$$R_n = R_d \times \begin{cases} 0.05\delta & \text{if } n=0 \\ \sinh(n\delta) & \text{otherwise,} \end{cases} \quad (20)$$

so  $R_{n+1} - R_n \simeq R_d \delta$  near the centre but far out we have  $R_n \simeq \frac{1}{2} R_d e^{n\delta}$  and  $R_{n+1}/R_n \simeq e^\delta$ . The grid employed had 300 nodes and extended to  $10R_d$  with  $\delta = \sinh^{-1}(10/299)$ .

<sup>1</sup> In a spherical potential orbits do not precess with the consequence that  $\dot{h} = 0$  must solve equation (13) when  $\Sigma = 0$ .

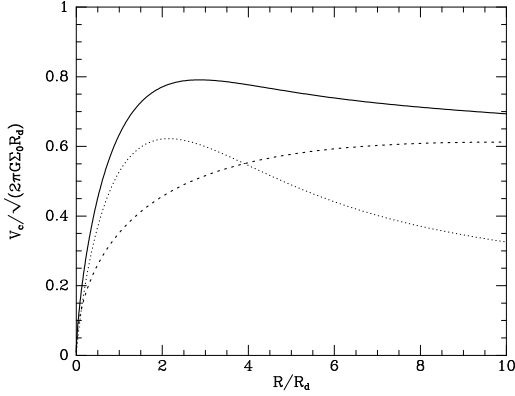


**Figure 1.** The full curve shows the circular-speed of the galaxy model used in Section 3. The contributions of the dark halo and the disc are shown by the dashed and dotted curves, respectively.

We force the innermost ring to remain in the plane by holding  $h_m(R_0) = 0$ .

By numerical integration we compute the values of  $N_m(R)$  at each grid point and store them. For each grid value of  $R$  we similarly compute and store the integral in equation (13) over each interval  $R' \in (R_j, R_{j+1})$  with  $h' - h$  replaced by the  $n$ th power of  $t = (R' - R_j)/(R_{j+1} - R_j)$  for  $n = 0, \dots, 3$ . At each timestep a cubic spline is fitted to the values of  $h_m$  on the grid and then the integral in equation (13) is evaluated as  $\sum_{in} M_i^n H_{in}$ , where  $H_{in}$  is the coefficient of  $t^n$  for the interval starting at  $R_i$  in the spline representation of  $h_m$ . The seventh-order Runge-Kutta algorithm is used to advance the  $h_m$  in time.

### 3 WARPING OF AN ISOLATED GALAXY

In this section we integrate the equations from a non-zero initial disturbance but without external stimulus such as that from the Sgr dwarf. These integrations both elucidate the physics of warps and enable us to check on the correctness of the code by evaluating the energy integral (C13) that is derived in Appendix C. We focus on the dipole component  $h_1$ , when stars populated rigid rings.

The dotted curve in Fig. 1 shows the circular speed generated by an exponential disc with an exponential surface-density profile

$$\Sigma(R) = \Sigma_0 e^{-R/R_d}, \quad (21)$$

while the dashed curve shows the circular speed of the dark halo adopted in his section. The combined circular-speed curve is not dissimilar to that of our own Galaxy. Notice that the orbital period at  $R = 3R_d$  is  $T_\phi = 2\pi R/v_c \simeq 3\pi\sqrt{R_d/G\Sigma_0}$ .

Fig. 2 shows the evolution of a disc that initially lies in different planes at small and large radii: at  $R < 2.5R_d$  the disc lies in  $z = 0$  while at  $R > 4.5R_d$  it lies in a plane that intersects  $z = 0$  along the  $x$  axis:

$$\Im h_1(R) = -h_{\max} \times \begin{cases} 0 & R < \bar{R} - \Delta \\ R/(\bar{R} + \Delta) & R > \bar{R} + \Delta \\ \frac{1}{2} \left( 1 + \sin \left[ \frac{\pi}{2\Delta} (R - \bar{R}) \right] \right) & \text{otherwise.} \end{cases} \quad (22)$$

with  $\bar{R} = 3.5R_d$  and  $\Delta = R_d$ . Here  $h_{\max}$  is an arbitrary constant that plays no role because we are doing linear theory.

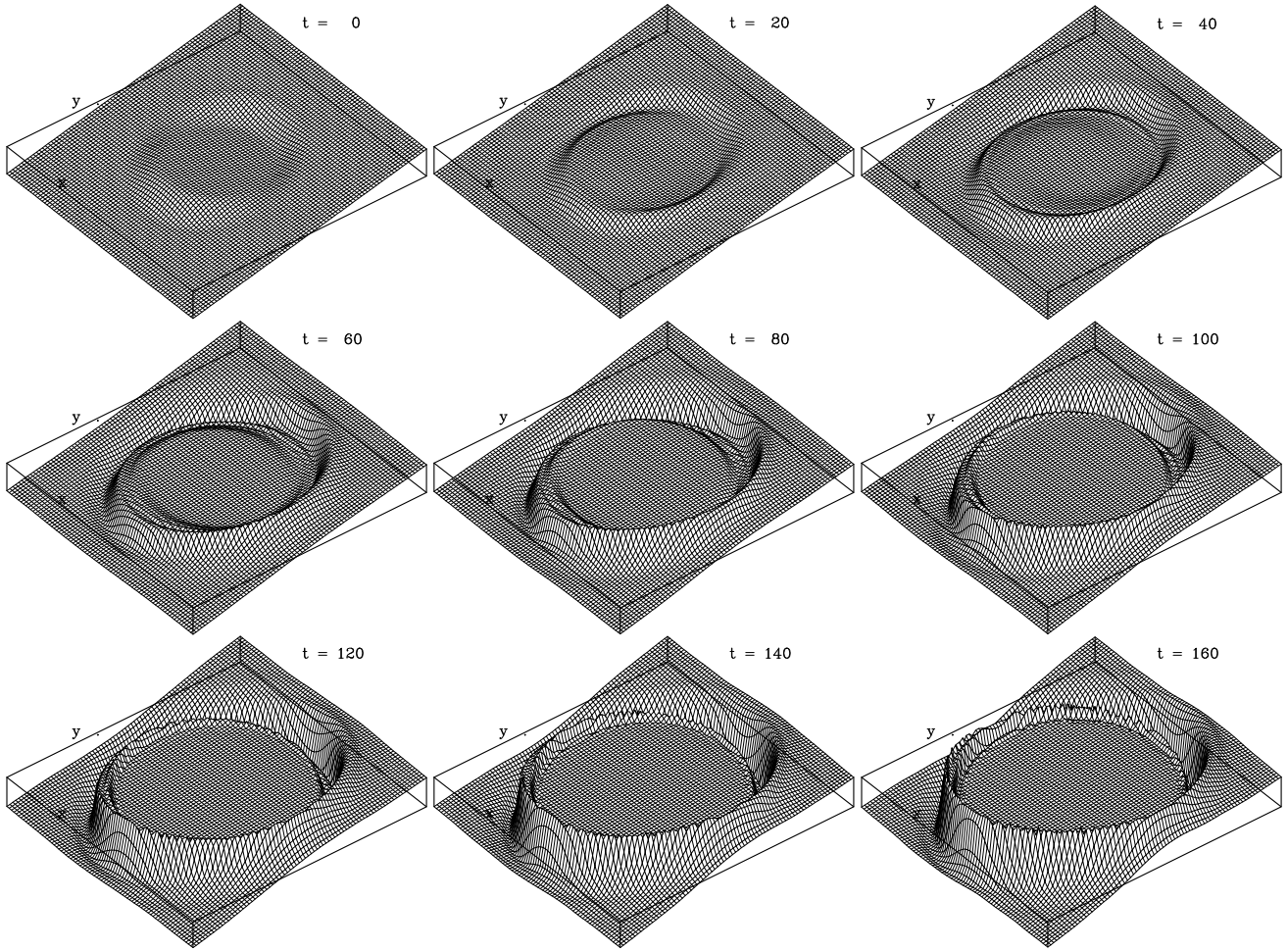
The top row of panels in Fig. 2 shows the evolution of the disc over the first 160 dynamical times  $\sqrt{R_d/G\Sigma_0}$ . The flat outer region torques the flat inner region about the  $x$  axis, while the inner region torques the outer region in the opposite sense about the same axis. Both regions respond to torques like gyroscopes by tilting around the  $y$  axis: in Fig. 2 the near part of the inner region moves downwards, while the furthest part moves upwards (Fig. 3). The rings that surround the inner disc move in the opposite direction and within the outer disc the line of nodes tilts away from the  $x$  axis in the opposite sense to the line of nodes across the inner disc.

The near edge of the outer region moves downwards. The torques are strongest at the inner and outer edges of the transition region in which  $h_1$  varies rapidly. The coupling between rings decays exponentially outwards with the surface density, so the inner region's rings remain almost coplanar by efficiently redistributing angular momentum that's acquired from the outer region. The outer rings are much less tightly coupled, with the result that the angular momentum acquired from the inner disc remains concentrated in the rings within and just outside the transition region. In consequence these rings precess (retrogradely) rather rapidly. In Fig. 2 the tipping and precession of these rings manifests as a bump on the near side and a trench on the far side.

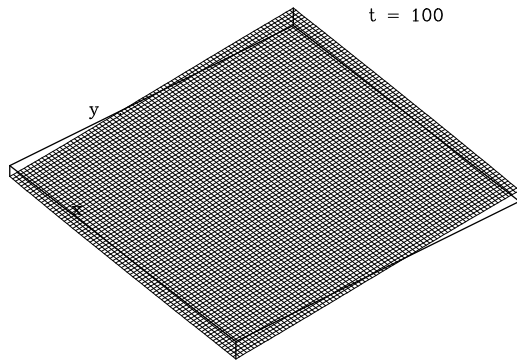
A better understanding of the evolution seen in Fig. 2 can be gained by examining plots of  $|h_1|/R$  and the angle  $\phi$  of the line of nodes as functions of time for representative rings. Fig. 4 plots these variables for six rings: two in the central region ( $R = R_d$  and  $R = 2R_d$ ), two that the transition region passes over ( $R = 4.5R_d$  and  $R = 5.5R_d$ ) and two in the outer region ( $R = 6.2R_d$  and  $R = 7R_d$ ).

The upper panel of Fig. 4 shows that  $|h_1|/R$  is initially constant over the outer three and rises only slowly later. This indicates that the tilts of these rings are consistent with them continuing to lie in the same inclined plane. By contrast, the two rings of the central region have  $|h_1|/R$  initially rising from zero and then flattening out to a common constant, signalling that from  $t \sim 60$  onwards the inner region settles to a flat disc that's inclined with respect to the coordinate system. The curve of  $|h_1|/R$  for the third ring from the centre ( $R = 4.5R_d$ ) starts from the value characteristic of the outer rings but from  $t \sim 30$  falls towards the steady value reached by the inner two rings. This behaviour reflects the spreading of the central, flat region that is evident in Fig. 2.

The lower panel of Fig. 4 shows the position angle of the lines of nodes from equation (15) for each of the six rings. The curves for the outer four rings start at 180 deg and fall at rates that decrease as  $R$  increases because a ring's precession rate decreases with  $R$ . The two innermost rings initially have undefined values of  $\phi$  because they lie in the plane  $z = 0$ , so their curves in Fig. 4 are initially erratic. By  $t \sim 10$ , the full curve for the innermost ring has settled to value around  $-70$  deg and from there it falls steadily towards  $\phi \sim -160$  deg. The curve for the next ring out,  $R = 2.5R_d$ , converges on the curve for  $R = R_d$  by  $t \simeq 40$ . Thus the inner disc tilts but ultimately does not precess. The curve for the ring with  $R = 4.5R_d$  falls rapidly until  $t \sim 120$ , and



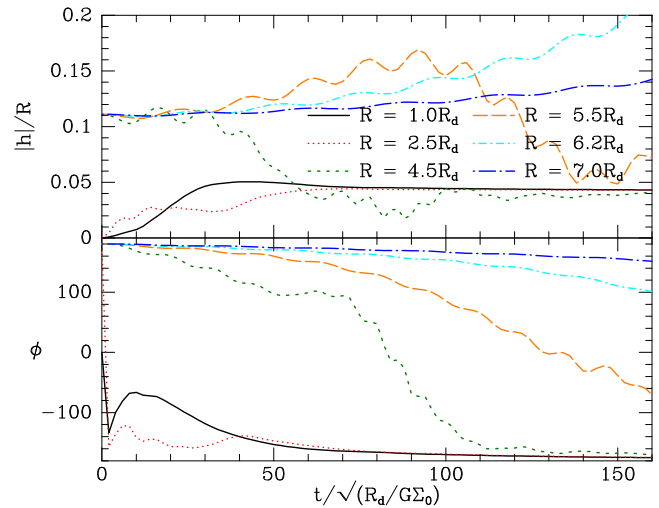
**Figure 2.** An  $m = 1$  disturbance in an exponential disc at the times given above in units of  $\sqrt{R_d/G\Sigma_0}$ . The plotted grid extends to  $x, y = \pm 7.1R_d$  while the radial grid used for the computation extends to  $R = 10R_d$ . The RMS variation of energy during the integration was 2.7 per cent.



**Figure 3.** The inner disc at  $t = 100$  is to good precision planar but tilted so the line of nodes makes an angle of 20 deg with the  $x$  axis. The largest ring contained within the square has  $R = 2.5R_d$ .

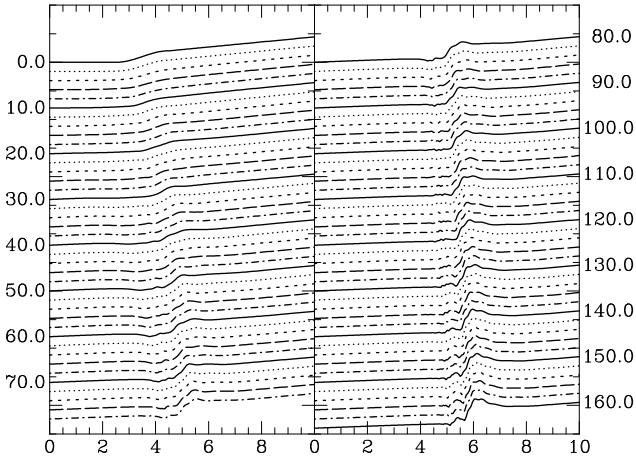
then oscillates around  $\phi = -155$  deg, reflecting this ring's absorption by the flat inner disc.

Fig. 5 provides a simpler perspective on the disc's evolution by plotting the amplitude  $|h_1|$  as a function of radius at a large number of times. Each curve has a well-defined step in the annulus within which the inner, flat disc transitions to



**Figure 4.** The warp's amplitude (upper panel) and line of nodes (lower panel) as functions of time on six selected rings.

the outer tilted disc. This region of transition moves steadily outwards – over 160 time units ( $\sim 5$  orbital periods at  $4R_d$ )



**Figure 5.** The amplitude of a corrugation with  $m = 1$  within a razor-thin exponential disc. Each curve shows the amplitude  $|h_1|$  as a function of  $R$  in kpc at a given time; successive curves are displaced downwards for clarity. The numbers down the left and right edges give the times in units of  $\sqrt{R_d/G\Sigma_0}$  of the nearest full curve.

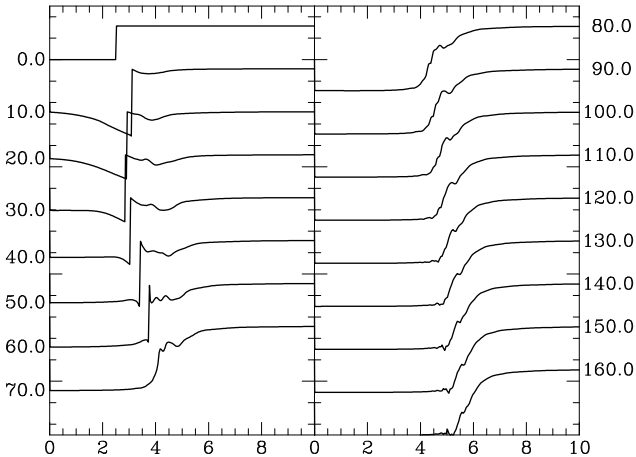


**Figure 6.** The angle  $\phi$  in the  $xy$  plane of the line of nodes from equation (15) as a function of ring radius in kpc. The times of the full curves are given along the left and right edges as in Fig. 5.

its centre moves from  $3.5R_d$  to  $5.75R_d$ . Inside the transition region, a small linear increase in  $|h_1|$  develops, because the inner disc tilts slightly while remaining almost flat. Outside the transition region, the initial linear increase of  $|h_1|$  with  $R$  fades between 80 and 160 time units. The length of the transition region does not change much.

Fig. 6 complements Fig. 5 by plotting the position angle  $\phi(R)$  of the line of nodes as a function of radius at a series of times. At  $t = 10$   $\phi$  varies quite rapidly in the inner disc, implying that the disc has a spiral structure. From  $t \sim 60$  torques have straightened the line of nodes in the inner disc.

Before  $t \sim 70$ , there are steps in  $\phi(R)$  that are caused by  $\phi$  moving through  $\pm 180$  deg. They can be banished by re-defining the definition of  $\phi$ , but with  $\phi$  redefined, the curves acquire step discontinuities at  $t > 60$ . Regardless of how  $\phi$  is defined, the orientation of the line of nodes swings rapidly from one side of the  $x$  axis to the other as  $R$  passes through the transition zone.

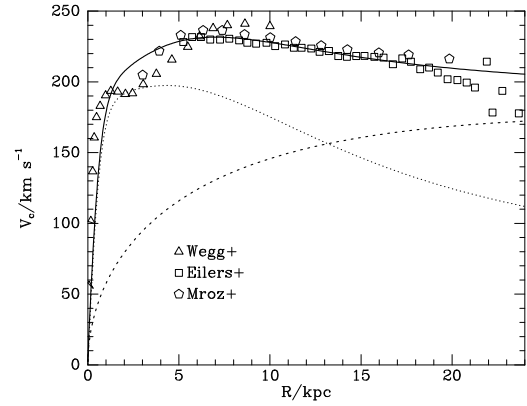


**Figure 7.** Full curve: the circular speed in the adopted Galaxy model. Dotted and dashed curves show the contributions of baryons and dark matter, respectively. The points show observational estimates from three studies.

**Table 1.** The current phase-space location of the Sgr dwarf.

$(\alpha, \delta)/\text{deg}$	$s/\text{kpc}$	$(\mu_\ell, \mu_b)/\text{mas yr}^{-1}$	$V_{\text{los}}/\text{km s}^{-1}$
(283.76, -30.48)	27	(-2.7, -1.35)	142

## 4 WARPING BY THE SGR DWARF

### 4.1 Orbit of the Sgr dwarf

Possible orbits of the Sgr dwarf have been explored by Dierickx & Loeb (2017), Vasiliev et al. (2021) and many others. Table 1 gives the current phase space coordinates of the Sgr dwarf from Vasiliev et al. (2021). We have integrated orbits of point masses in the Galaxy’s potential to find one that comes close to this location. For simplicity, we assume the Galaxy’s potential is spherical, with contributions from a Hernquist (1990) sphere, a disc and a bulge. At the radii explored by the Sgr dwarf, the potentials of the disc and bulge can be approximated by those of point masses and we have used this approximation. The mass and scale length of the Hernquist sphere are chosen such that, after addition of the (not necessarily spherical) potentials of the model disc and bulge listed in Table 2, we obtain the fit to the Galaxy’s circular-speed curve that is shown in Fig. 7.

The assumption of spherical symmetry confines the dwarf’s orbit to an orbital plane. We compute orbits in the presence of dynamical friction, computed from equation (8.3) in Binney & Tremaine (2008) using the sphere’s ergodic DF (eqn. 4.51 in Binney & Tremaine).

Tidal stripping of the dwarf’s mass was computed by modelling the dwarf as a Hernquist sphere of mass  $m$  and

**Table 2.** Models of the Galaxy’s disc and bulge

Component	Type	mass $10^{10} M_\odot$	scale length kpc
Disc	exponential	5	3
Bulge	Plummer sphere	1.5	1
Dark halo	Hernquist sphere	100	35

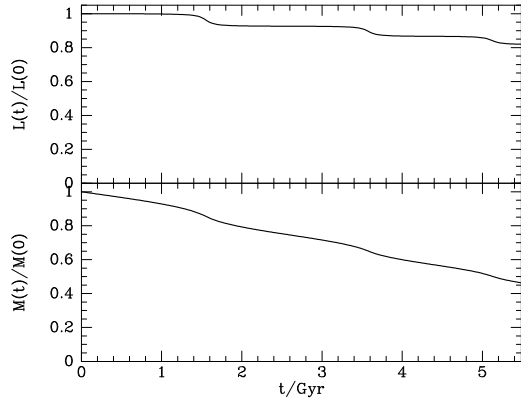


**Figure 8.** The dwarf’s angular momentum (upper panel) and mass (lower panel) along the orbit shown in Fig. 9.

scale radius  $a$ . At each timestep, the dwarf’s tidal radius  $r_t$  was computed from the equation

$$\frac{m}{(r_t + a)^2 r_t} = \frac{M}{(R + A)^2 R}, \quad (23)$$

where  $M$  and  $A$  are the mass and radius of the Galaxy’s halo and  $R$  is the distance between the centres of the dwarf and the Galaxy. Equation (23), which can be expressed as a cubic that typically has only one real root, equates the acceleration at radius  $r_t$  generated by the dwarf to the difference in the forces applied by the Galaxy at  $r_t$  and at the dwarf’s centre. Let  $m(t)$  be the dwarf’s mass at time  $t$  and let  $M_t$  be the mass within  $r_t$  of a Hernquist sphere of total mass  $m$ , and scale radius  $a = 5$  kpc, i.e.,

$$M_t = m(t) \left( \frac{r_t}{r_t + a} \right)^2. \quad (24)$$

Then we have evolved  $m$  by solving

$$\frac{dm}{dt} = -\frac{m - M_t}{T_{\text{strip}}}, \quad (25)$$

where  $T_{\text{strip}}$  is a constant of order a gigayear. This procedure acknowledges that material that lies outside  $r_t$  does not instantly vanish, while material that at time  $t$  lies inside the tidal radius will eventually be stripped. The lower plot of Fig. 8 shows how  $m$  decreases with time along our favoured orbit, which is obtained with  $T_{\text{strip}} = 2$  Gyr. The decline steepens slightly at each pericentre – corresponding but clearer features are visible in the plot of angular momentum versus time in the upper panel of Fig. 8.

Fig. 9 shows our orbit in real space on the left and in velocity space on the right. Black dots mark initial conditions and crosses mark the observed location of the Sgr dwarf; squares mark pericentres. 35 Myr after its third pericentre and 5.156 Gyr since the start of the integration, the orbit passes close to the dwarf’s observed location. This orbit was obtained by setting  $m(0) = 5 \times 10^{10} M_\odot$  and taking the Coulomb logarithm to be  $\ln \Lambda = 6$ , but the orbit depends only on the product  $m(0) \ln \Lambda$ .

The orbit is computed as a planar object in the approximation that the Galactic potential is spherical, and is then rotated into the frame that’s aligned with the Galactic disc and places the Sun on the negative  $x$  axis. At any given time the tidal acceleration  $\mathbf{g}$  can now be computed from equation (18) and Fourier decomposed (eq. 19). The

**Table 3.** Pericentres along the dwarf’s orbit. The dwarf reaches its current location at  $t = 5.156$  Gyr.

	Peri 1	Peri 2	Peri 3
$r$ (kpc)	22.32	21.54	20.92
$t$ (Gyr)	1.552	3.578	5.121

lower panel of Fig. 10 shows the Galactocentric radius of the dwarf as a function of time. The pericentric radii, given in Table 3, decrease remarkably slowly. The near constancy of the pericentric radii reflects much faster loss of energy than of angular momentum. This in turn reflects the density profile of the Galaxy’s dark halo: since a tangential force  $F$  causes energy and angular momentum to change at rates  $\dot{E} = vF$  and  $\dot{L} = rF$ , at peri- or apocentre, the rates of loss of  $E$  or  $L$  are in the ratio

$$\frac{\dot{E}}{\dot{L}} = \frac{v}{r}, \quad (26)$$

where  $v$  is the dwarf’s speed and  $r$  is its Galactocentric radius. The ratio  $v/r$  is much bigger at pericentre than at apocentre, so drag at pericentre tends to circularise the orbit, while drag at apocentre has the opposite tendency. Our use of a Hernquist dark halo, which has an asymptotic variation of density  $\rho \propto r^{-3}$  rather than that  $\rho \propto r^{-2}$  characteristic of an NFW density profile (Navarro et al. 1997) favours circularisation. We have, however, checked that computing friction from an NFW profile has a negligible effect on the evolution of the pericentres, probably because the dwarf’s orbit spans the scale radius  $a = 35$  kpc around which the slope of the logarithmic density profile transitions from  $-1$ .

The upper panel of Fig. 10 shows the coefficient of  $\cos \phi$  in the dipolar component of the tidal acceleration on the ring of radius  $R = 12$  kpc – the coefficient of  $\sin \phi$  is significantly smaller. We see that the forcing is very tightly concentrated around pericentres. Fig. 11 reveals that around each pericentre the monopole and quadrupole contributions to tidal forcing are not much smaller than the dipole contribution. This finding may explain why the distortion of our Galaxy’s HI distribution requires significant contributions from monopole and quadrupole terms (cf Binney & Merrifield 1998, eq. 9.18).

## 4.2 Warp excited by the dwarf

Since the Galaxy rotates clockwise when viewed from the north, in the equations of motion (13) we take  $\Omega < 0$ . Within the Galactic plane we use polar coordinates  $(R, \psi)$  with  $\psi$  increasing in the direction of Galactic rotation.

Fig. 12 shows the amounts  $z(\psi)$  by which the stars are pulled from the plane at four times around the dwarf’s first pericentre: the curves show the values of  $z$  obtained by averaging the Fourier coefficients  $h_i$  for  $i \leq 2$  over annuli 3 kpc wide that are centred on  $R = 12, 16, 20$  and 24 kpc. The grey bands show the standard deviations of  $z$  within these annuli, which are readily calculated from the mean values of  $h_i$  and  $|h_i|^2$ . The distortions are very small until the dwarf reaches pericentre at  $t \sim 1.6$  Gyr. Then it grows rapidly at  $R \gtrsim 10$  kpc, and by 1.7 Gyr it reaches 2 kpc at  $R \sim 24$  kpc. The subsequent development comprises a train of waves that moves outwards whilst shifting to shorter wavelengths. As

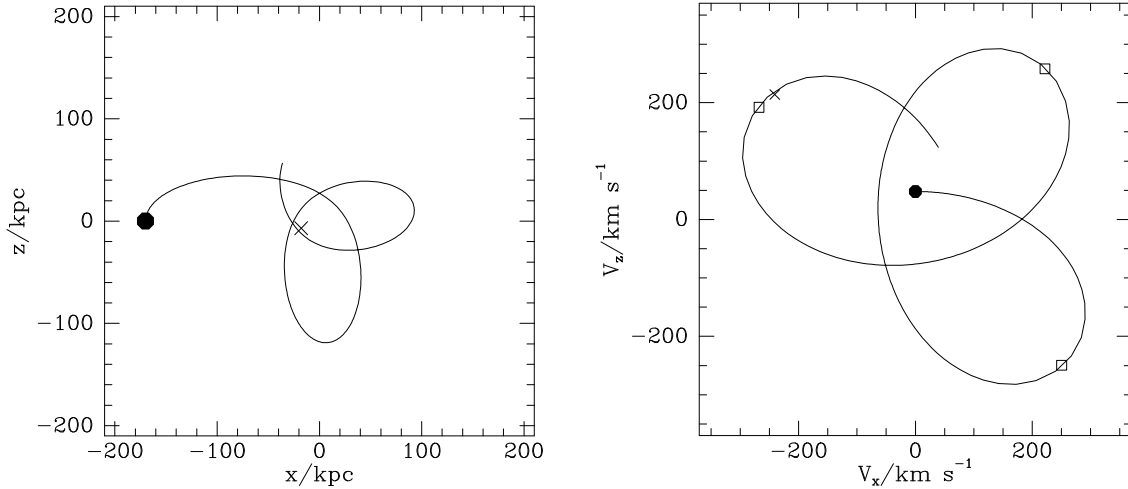


**Figure 9.** A possible orbit of the Sgr dwarf in real space (left) and velocity space (right). The black dots show the initial conditions chosen, while the crosses show the observed location of the dwarf. Pericentres are marked by open squares.

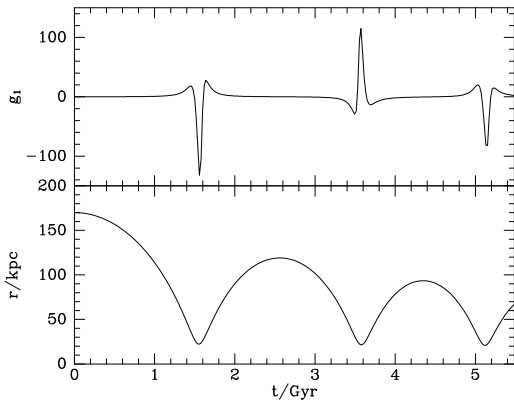


**Figure 10.** Galactocentric radius (lower panel) and dipole forcing at  $R = 12$  kpc (upper panel) as functions of time along the orbit shown in Fig. 9. The units of  $g_1$  are  $M_{\odot} \text{pc}^{-2}$ .

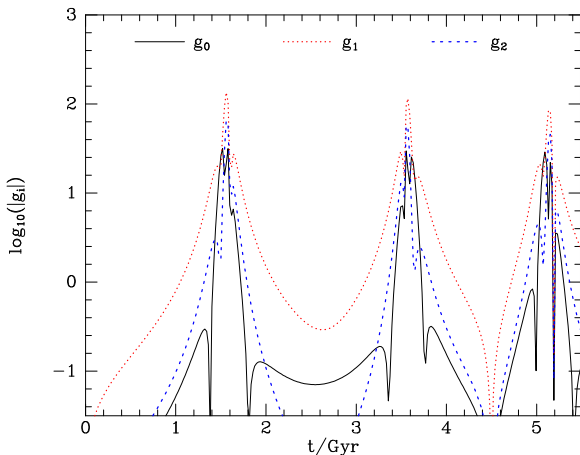


**Figure 11.** The magnitudes of the monopole (full curve), dipole (dotted curve) and quadrupole (dashed curve) contributions to tidal forcing of the Galactic disc at  $T = 12$  kpc by the Sgr dwarf. The units of  $g_m$  are  $M_{\odot} \text{pc}^{-2}$ .

the dwarf moves away, the radially-averaged amplitude of the vertical oscillations slowly diminishes at any given radius through phase mixing and the outward transport of energy by waves. Fig. 13 illustrates this result by showing the mean and standard deviation of  $z(\psi)$  within the annuli at 2.8 Gyr, that is shortly after the dwarf's second apocentre. The curves show smaller amplitudes of oscillation than in the bottom-right panel of Fig. 12 while the widths of the grey bands have changed very little.

Fig. 14 shows a three-dimensional representation of the disc at six times spanning 0.7 Gyr from about the first pericentre. The highest point moves clockwise by almost a quarter turn in the 0.1 Gyr that separates the first four snapshots and has completed a more than a complete turn by the fifth snapshot at  $t = 2.1$  Gyr. Near the centre we see a flat region that slowly expands and is bounded by crests and troughs that form a two-armed trailing spiral that becomes rapidly tighter. The overall effect is to create a stadium in which a flat playing field is surrounded by tiers of an ever-increasing number of benches that become steadily narrower.

The pericentre that provokes the response plotted in Fig. 14 lies  $\sim 3.5$  Gyr in the past, so the winding up process that is already advanced in the final snapshot would by now have brought peaks and troughs so close to one another that the in-plane epicycle motion of stars that is absent from the model would have completely blended peaks and troughs into a smooth, warp-free disc that has become thick outside the central flat region. In other words, the long-term effect of the first pericentre is to make an initially thin disc into one that flares strongly at the edge of the central flat region. Fig. 15 shows as a function of time the standard deviation  $\Delta_z$  of  $z(R, \phi)$  within annuli that are 2 kpc wide and centred on  $R = 8, 12, 16, 20$  and 24 kpc. We should interpret  $\Delta_z$  as the disc thicknesses that result from the winding up of the warp that the dwarf induces as it orbits through its last three pericentres. We see that at  $R = 24$  kpc  $\Delta_z$  shoots up just before the dwarf passes through its first pericentre at  $t \sim 1.5$  Gyr. By  $t = 2$  Gyr the sharp upward movement of  $\Delta_z$  has flattened to a gradual upward drift to  $\sim 1.5$  kpc on which are superposed oscillations that have a period  $\sim 0.4$  Gyr. The behaviour of  $\Delta_z$  at  $R = 20$  and



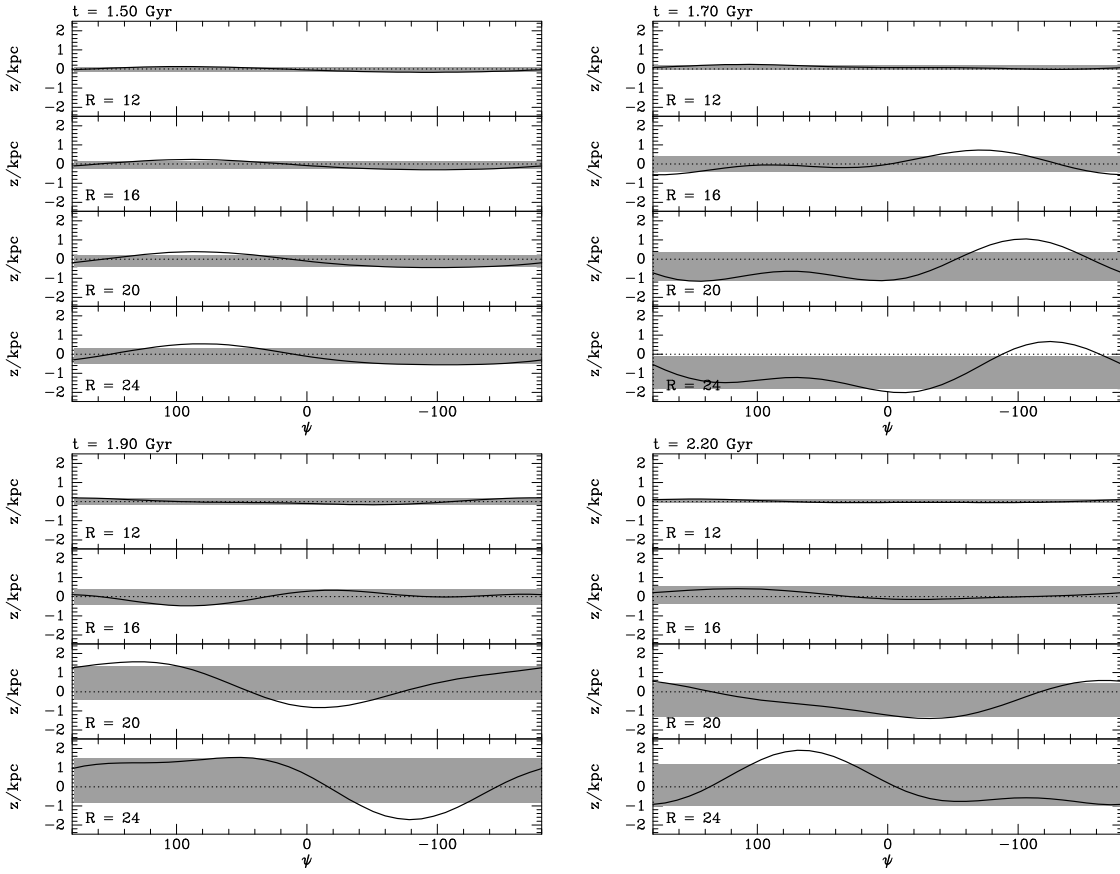


**Figure 12.** Amounts  $z(\psi)$  by which stars are pulled from the plane averaged over four annuli centred on  $R = 12, 16, 20$  and  $24$  kpc, containing 24, 18, 15 and 12 rings, respectively. The curves are plotted from the values of  $h_0$ ,  $h_1$  and  $h_2$  radially averaged with weight  $e^{-R/5 \text{ kpc}}$ , while the grey bands show the corresponding standard deviations of  $z$ . The times, given at top left of each panel, span the dwarf’s first pericentre. The angle  $\psi$  increases in the direction of Galactic rotation.

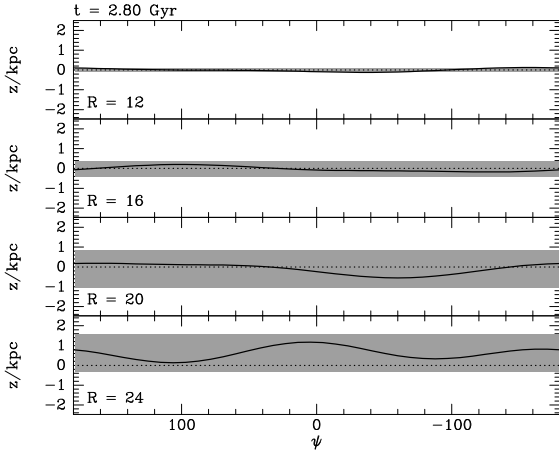


**Figure 13.** The distortion of the disc at  $t = 2.8$  Gyr, shortly after the dwarf’s second apocentre. The meaning of the curves and bands is as in Fig. 12.

16 kpc is similar although the level reached at  $t = 2$  Gyr is smaller, especially at  $R = 16$  kpc, and the later oscillations have smaller amplitude and a shorter period. For these radii it’s just possible to detect upwards steps in  $\Delta_z(t)$  around the times, 3.5 Gyr and 5.15 Gyr, of the dwarf’s second and third pericentres. At  $R = 8$  kpc and 5 kpc (not plotted)  $\Delta_z$

remains less than 0.1 kpc throughout. At 12 kpc  $\Delta_z$  is currently  $\sim 0.2$  kpc, which is significantly less than the half thickness of the low- $\alpha$  disc near the Sun.

Figs. 12 to 15 thus lead to the conclusion that soon after a pericentre, a warp develops that co-rotates with the stars and winds up from inside out. In the long run the pericentre produces an axisymmetric but flaring disc. For only  $\sim 0.3 - 0.4$  Gyr from pericentre will a warp will be evident. In light of this conclusion we now focus on the effect that the most recent pericentre has on the gas disc, because we expect viscous damping to re-establish a thin gas disc after each pericentre. Moreover the configuration of the gas disc far beyond the solar circle is better constrained by observations than is the configuration of the outer reaches of the stellar disc.

The upper panel of Fig. 16 shows the disc as it would be now if it had been flat  $\sim 0.95$  Gyr ago as the Sgr dwarf moved past its last apocentre. The following pericentre would have generated a warp that depresses the disc in the direction of Galactic rotation i.e., right back in Fig. 16. The lower panel of Fig. 16 shows the  $m = 1$  component of the fit to observations of the Galaxy’s HI disc given in Binney & Merrifield (1998). At a qualitative level the agreement between model and fit to data is good: model and fit agree on the extent of the disc’s flat portion, and that the line of nodes of the large-scale warp falls near the  $x$  axis (on which the Sun lies).

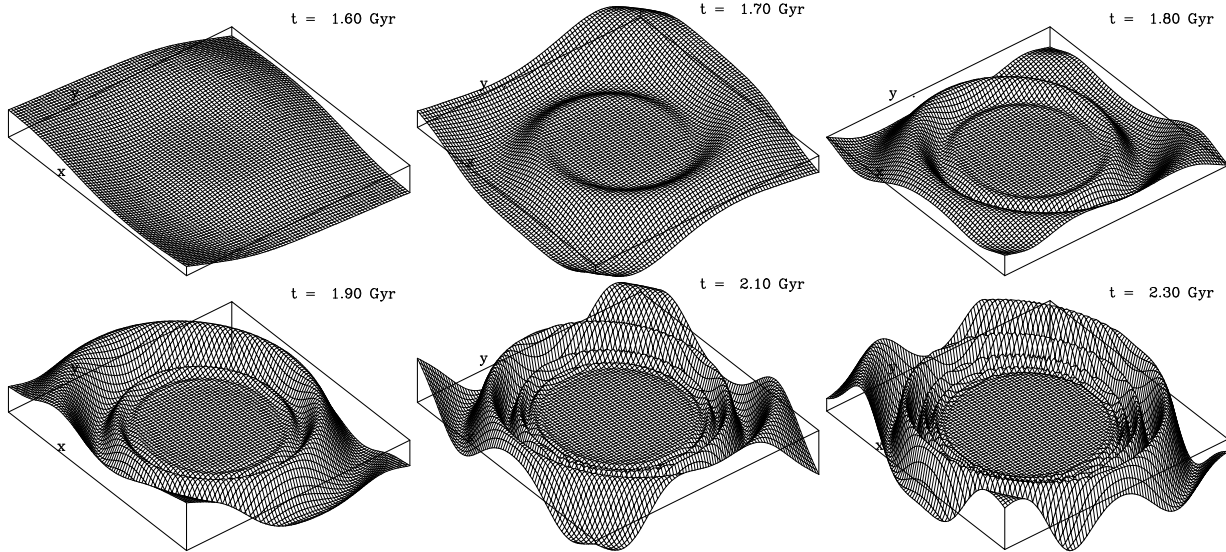


**Figure 14.** The component  $m = 1$  of the distortion that is induced in the Galactic disc by the Sgr dwarf galaxy at its first pericentre. The squares are 42.4 kpc on a side so they completely contain rings out to radius 21.2 kpc.

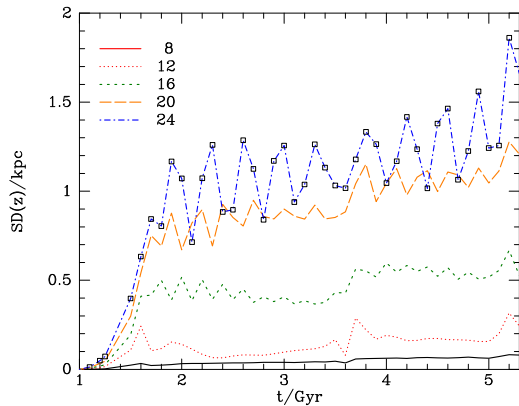


**Figure 15.** Each curve shows the evolution of the standard deviation of  $z$  in an annulus 2 kpc wide as the dwarf's orbit is integrated from  $t = 1$  Gyr to  $t = 5.3$  Gyr, which is about 150 Myr into the future. The central radius of each annulus is shown at top left. In the case of the curve for  $R = 24$  kpc, times at which  $\Delta_z$  has been calculated are marked by squares. These times apply to all curves.

The figure conceals a significant difference, however, by using scales for  $z$  that differ by a factor three: the amplitude of the observed warp is three times larger than that of the model warp. There are several possible explanations of this discrepancy, as we discuss below.

Fig. 17 plots the model's prediction for the location  $z(\psi)$  of the middle of the gas layer around three annuli,  $R = 12, 16, 20$  and 24 kpc. These plots may be compared with Figure 9.24 in Binney & Merrifield (1998), which shows the estimated density  $n(z, \psi)$  of HI within cylindrical shells.<sup>2</sup> The model captures the asymmetry between positive and negative values of  $\psi$ , which is defined so it increases in the direction of Galactic rotation and the sun lies

<sup>2</sup> The caption to Figure 9.24 is in error: the Sun lies at  $\psi = \pm 180$  deg, not at 0.

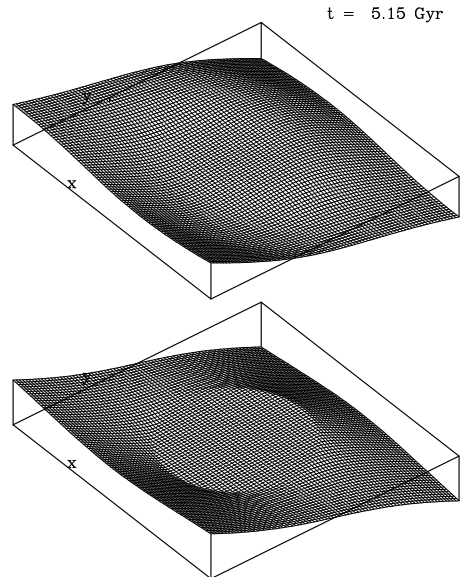


**Figure 16.** Upper panel: the  $m = 1$  structure of the disc at  $t = 5.15$  Gyr after an initially flat disc has been evolved from  $t = 4.6$  Gyr through the most recent pericentre of the Sgr dwarf. Lower panel: the  $m = 1$  component of the model fitted to HI data by Binney & Merrifield (1998).

on  $\psi = \pm 180$  deg. The model also captures much of the growth with  $R$  of the amplitude of the warp.

When the equations are integrated into the future, the warp is seen to change rapidly: the central region becomes flatter and more sharply demarcated from the outer region, and the latter becomes corrugated rather than warped.

## 5 DISCUSSION

The vertical dynamics of galactic discs are a potentially fruitful area, not least for the light they could shine on den-

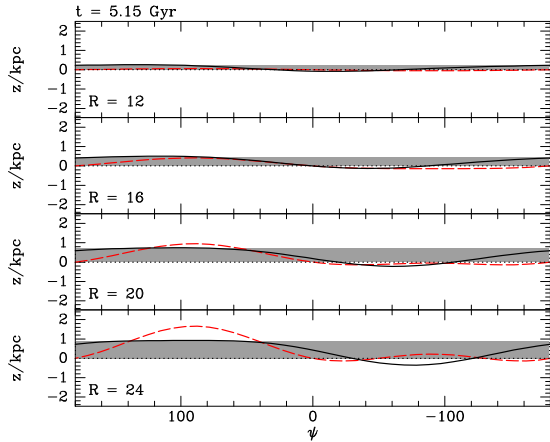


**Figure 17.** Plots of  $z(\psi)$  at four radii at the current time according to the model of the effect of the Sgr dwarf. The dashed red curves show  $z(\psi)/3$  where  $z(\psi)$  is the fit of equation (9.18) in Binney & Merrifield (1998) to the model of the Galactic HI layer depicted in their Figure 9.24.

sity fluctuations in dark haloes. Unfortunately, this is an exceptionally challenging area of stellar dynamics because the vertical oscillations of stars are strongly anharmonic and inherently coupled to their in-plane motions. Moreover, we suffer from a want of sufficiently accurate analytical expressions for the gravitational potential of a distorted disc of finite thickness. Consequently our options seem to be (i) brute-force N-body simulation (e.g. Laporte et al. 2018; Bland-Hawthorn et al. 2019; Bland-Hawthorn & Tepper-Garcia 2021), which is expensive and cumbersome, (ii) evolving non-equilibrium distribution functions in a fixed model potential  $\Phi(z)$  (e.g. Binney & Schönrich 2018; Tremaine et al. 2023), which is very restrictive, and (ii) as here, modelling a disc by stars on perfectly circular orbits, which excludes any discussion of the distributions of stars in the  $(z, v_z)$  phase plane.

This phase plane has recently attracted a lot of attention following the discovery by Antoja et al. (2018) of a spiral in the  $(z, v_z)$  distribution of stars near the Sun. Unfortunately, it's logically impossible to deduce the impact of a perturber such as the dwarf on the  $(z, v_z)$  distribution of stars without computing the bodily acceleration of the disc at each radius by the combined gravitational pulls of the perturber, the rest of the disc and the dark halo. The focus of the present paper has been precisely on this larger-scale dynamics which should logically precede discussion of dynamics within  $(z, v_z)$  phase planes.

Our discussion of the evolution of a free warp in Section 3 was instructive but limited in scope by the initial conditions having  $\dot{h} = 0$ . It is likely that other, possibly more interesting, behaviour will emerge when  $\dot{h}$  is chosen differently. In the case of a violin string, setting  $\dot{h}$  to zero is equivalent to specifying initial conditions that comprise two waves that differ only in their direction of travel. Our observation in Section 3 that the disturbance seems to move outwards could be considered to confound this expectation. A disturbance *does* move inwards, however, but it tips the inner disc in an orderly fashion rather than generating tightly-wound corrugation waves.

Probably the most important uncertainties in Section 4

concern the mass and shape of the Sgr dwarf. At early times the dwarf's mass has to be of order  $10^{11} M_\odot$  if it is to experience enough dynamical friction to get onto its present orbit (Jiang & Binney 2000). We have rather arbitrarily adopted  $5 \times 10^{10} M_\odot$  as initial mass and our algorithm for mass loss causes the mass to fall to  $1 \times 10^{10} M_\odot$ , which is quite a large value given the dwarf's current luminosity  $L \sim 10^8 L_\odot$  (Niederste-Ostholt et al. 2012). Clearly, changes in the dwarf's mass will translate immediately to changes in the amplitude of the warp it generates.

An equally serious uncertainty is the location of the dwarf's mass. A significant fraction of the dwarf's stars have already been stretched into a stream that wraps more than once around the Galaxy. The dwarf's dark matter is even more liable to shredding into a stream and we ought really to be computing the response of the disc to a stream that spreads while moving its centre along the computed orbit.

We have compared our dynamical model to observations by way of a fit to a model of the HI distribution. The HI model was fitted by Voskes & Burton (1999) to a composite data cube extracted from the surveys of Hartmann & Burton (1997), Weaver & Williams (1974) and Kerr et al. (1986). The model specifies the density  $n(z, \psi)$  of neutral hydrogen in a series of annuli. Extracting such a model from the observational data cubes is not straightforward and Voskes & Burton never published a full account of their work – the fit we have used is based on four plots that Voskes and Burton provided for publication in Binney & Merrifield (1998). The model relies on distances to emitting hydrogen that assume that the Sun's radius  $R_0 = 8.5$  kpc and the circular speed is constant at  $220 \text{ km s}^{-1}$ . It follows that the HI model, and its analytic fit do not have the status of fact.

A dynamical model would be better compared with HI data by using the model to generate a mock HI data cube. The drawback of this procedure is the difficulty of displaying the quality of fits in a three-dimensional space, but this procedure should nonetheless be tried soon.

A major issue is that the dynamical model produces an amplitude that is three times smaller than observations seem to require, even though it is based on a model of the dwarf that is surely too concentrated and would be expected to over- rather than under-estimate its effect on the disc. The model has, however, two shortcomings that likely lead to under-estimation of the disc's response.

- One is failure to model the dynamical response of the dark halo, which we have assumed to be spherical rather than flattened. The halo must respond strongly to the dwarf – and the model exploits this response in as much as it gives rise to dynamical friction – but our equations of motion (13) completely ignore the halo's response. Weinberg (1989) explains how to compute the wake and shows that its structure is materially modified when the wake's self-gravity is taken into account. It's worth noting that self-gravity *reduces* the frictional drag to which the wake gives rise, by reducing the offset between the wake's barycentre and the perturber's location. Consequently, our treatment either over-estimates the frictional drag or under-estimates the dwarf's mass.
- Another questionable feature of the model is its assumption that the HI is part of a razor-thin disc with a strictly exponential surface density that is extrapolated from the *stellar* surface density near the solar circle. We are cer-

tain that the dwarf’s latest pericentre is not its first, and we have argued that the first pericentre caused the disc to flair strongly from  $R \sim 4R_d$ . After this first pericentre, the model applies only to the gas disc, which has a much lower surface density than the model assumes. On account of its low surface density, the gas disc is much less strongly stiffened by gravity than the model assumes, and will consequently respond more strongly to the current pericentre.

## 6 CONCLUSIONS

Section 2 offers a derivation of the equations of motion for the vertical dynamics of a razor-thin disc that differs in significant respects from that given by HT69. The principal difference is the use here of standard cylindrical polar coordinates rather than the confocal ellipsoidal system employed in HT69, but the equations derived are not mere transcriptions of the old equations between coordinate systems. The infinitesimal thickness of the disc gives rise to subtle questions about limits when one generalises from a series of discrete rings to a continuous disc. We have formulated equations which yield finite values for the quantities required for the equations of motion even in the continuum limit.

The change of coordinate system frees the disc from the requirement to lie within the infinitely-flattened ellipsoid of the confocal system, and therefore make it possible to discuss the dynamics of a standard exponential disc. The disc’s potential can be computed in this system quite cheaply thanks to the Green’s function that Cohl & Tohline (1999) introduced.

Section 3 illustrated the tendency of warps to wind up into corrugation waves that propagate outwards, leaving the inner, higher-density, part of the disc flat. In Section 4 we presented a highly idealised model of the interaction of the Sgr dwarf with the Galactic disc. The tidal field of the dwarf is strongly concentrated around the pericentres of the dwarf’s orbit. The current phase-space coordinates of the dwarf imply that the dwarf has passed at least three pericentres, and the radii of successive pericentres decrease extremely slowly because, for any plausible structure of the Galaxy’s dark halo, the dwarf’s orbit circularises. From this it follows that the decisive pericentre must have been the first one, at least 3.6 Gyr ago. It seems that then the stellar disc beyond  $\sim 4R_d$  must have been thickened as the corrugation waves generated by the dwarf wound up. This conclusion chimes with accumulating evidence that near the solar circle the ‘thick disc’ transitions from being a high- $\alpha$  structure to a low- $\alpha$  structure (Schuster et al. 2012; Binney & Vasiliev 2023). An alternative, and probably better, perspective on the data is that just outside solar circle, the low- $\alpha$  disc suddenly flares into a thick structure just as our model requires.

In light of the likely disruption of the outer thin disc  $\gtrsim 3.6$  Gyr ago, our razor-thin model disc can be applied to the dwarf’s latest pericentre only by treating it as a model of the HI layer, which we expect to re-form into a thin disc after each disruption.

Considering the crudeness of the model and the number of poorly constrained parameters involved, the extent of the agreement between theory and observation in Figs. 16 and 17 is encouraging. The amplitude of the response is a factor

three smaller than the HI data imply but an under-estimated amplitude is to be expected in view of the model’s assumption of an unrealistically high surface density for the gas disc and a rigid halo. What is gratifying is the extent to which the model captures the complex shape of the warp, which has significant  $m = 0$  and  $m = 2$  components in addition to the dominant dipole component. Moreover, the warp’s shape evolves remarkably quickly and it agrees with the observed shape rather fleetingly. It’s striking that the moment of agreement coincides precisely with the moment that the dwarf passes through its observed phase-space location.

This investigation suggests several avenues for further investigation.

- Add the Magellanic Cloud system to the problem. This would be simple if the Cloud system were modelled in the same way as the dwarf, namely as a Hernquist sphere of mass  $\sim 10^{11} M_\odot$  that orbits a spherical model of the Galaxy as if it were a point particle. Weinberg & Blitz (2006) long ago argued that when tidal distortion of the dark halo is taken into account, the Cloud system acting alone can account for the outer gas warp. Recently it has been argued that the Cloud system significantly perturbs the orbits of objects such as globular clusters that orbit in the distant halo (Erkal et al. 2019). Hence it is likely that they have a non-negligible effect on the disc at  $R \gtrsim 20$  kpc even if their effect is small closer to the Galactic centre.

- Model the dwarf as a series of Hernquist spheres that move on slightly different orbits, so they are now spread roughly along the central orbit of the family. A model along these lines would be significantly more realistic than that presented here but almost as tractable. Since each component would pass through pericentre at a different time, the overall effect would be the extend the period over which the disc is disturbed, while holding the aggregate effect roughly constant.

- Include the effect on the disc of the wake that trails the dwarf as it moves through the Galaxy’s dark halo. The structure of such a wake has been computed by Mulder (1983), Weinberg (1993) and others.

- Compute the impact that the dwarf has on the  $(z, v_z)$  phase plane at a given azimuth  $\phi$  and radius  $R$ . This is a challenging task for two reasons: (i) one has to work in the non-inertial frame of the barycentre of the stars at  $R$ . This frame might reasonably be supposed to be frame defined by the HT69 star at  $(R, \phi)$ . By definition the frame’s acceleration cancels the gravitational field at the particle’s location that is jointly generated by the dwarf and our Galaxy. What has to be computed is the difference between the frame’s acceleration and the gravitational field at nearby points. This might be estimated by supposing that the middle of the vertical profile of a realistically thick disk lies in the surface  $z(R, \phi)$  computed here in the razor-thin approximation.

- Integrate the equations for  $h(R)$  from  $h = \dot{h} = 0$  in the case that the disc is embedded in a live dark halo that is out of equilibrium in the sense that it comprises spheroidal shells, the symmetry axes of which point in directions that shift as the shell’s increases. Han et al. (2023) presents an investigation that is similar, but suffers from the crucial limitation of a dead halo.

Although an enormous amount of work is required before we can be sure that we have solved the half-century old

puzzle of warps, this re-visit to the ideas of a classic paper strengthens the case that the Galactic warp is largely generated by the dwarf's tidal field. When this idea has been put on a more secure and quantitative basis, the warp phenomenon will surely provide valuable probes of both dark haloes and stellar discs.

## ACKNOWLEDGEMENTS

It's a pleasure to thank Sacha Guerrini for clarifying the discussions that clarified the work of Hunter & Toomre. This research was supported in part by grant NSF PHY-2309135 to the Kavli Institute for Theoretical Physics (KITP).

## DATA AVAILABILITY

The computations were performed by C++ code linked to the AGAMA library (Vasiliev 2019). The code is available upon request.

## REFERENCES

- Antoja T. et al., 2018, *Nat*, 561, 360  
 Binney J., Jiang I.-G., Dutta S., 1998, *MNRAS*, 297, 1237  
 Binney J., Merrifield M., 1998, *Galactic astronomy*. Princeton University Press  
 Binney J., Schönrich R., 2018, *MNRAS*, 481, 1501  
 Binney J., Tremaine S., 2008, *Galactic Dynamics: Second Edition*. Princeton University Press  
 Binney J., Vasiliev E., 2023, *MNRAS*, 520, 1832  
 Bland-Hawthorn J. et al., 2019, *MNRAS*, 486, 1167  
 Bland-Hawthorn J., Tepper-García T., 2021, *MNRAS*, 504, 3168  
 Bosma A., 1978, PhD thesis, University of Groningen, Netherlands  
 Briggs F. H., 1990, *ApJ*, 352, 15  
 Burke B. F., 1957, *AJ*, 62, 90  
 Cohl H. S., Tohline J. E., 1999, *ApJ*, 527, 86  
 Dierickx M. I. P., Loeb A., 2017, *ApJ*, 847, 42  
 Erkal D. et al., 2019, *MNRAS*, 487, 2685  
 Gaia Collaboration et al., 2023, *A&A*, 674, A1  
 Han J. J., Conroy C., Hernquist L., 2023, *Nature Astronomy*, 7, 1481  
 Hartmann D., Burton W. B., 1997, *Atlas of Galactic Neutral Hydrogen*. Cambridge University Press  
 Hernquist L., 1990, *ApJ*, 356, 359  
 Hunter C., Toomre A., 1969, *ApJ*, 155, 747  
 Jiang I.-G., Binney J., 2000, *MNRAS*, 314, 468  
 Kerr F. J., 1957, *AJ*, 62, 93  
 Kerr F. J., Bowers P. F., Jackson P. D., Kerr M., 1986, *A&AS*, 66, 373  
 Laporte C. F. P., Johnston K. V., Gómez F. A., Garavito-Camargo N., Besla G., 2018, *MNRAS*, 481, 286  
 Lau J. Y., Binney J., 2021, *MNRAS*, 507, 2241  
 McMillan P. J. et al., 2022, *MNRAS*, 516, 4988  
 Mulder W. A., 1983, *A&A*, 117, 9  
 Navarro J. F., Frenk C. S., White S. D. M., 1997, *ApJ*, 490, 493  
 Nelson R. W., Tremaine S., 1995, *MNRAS*, 275, 897

- Niederste-Ostholt M., Belokurov V., Evans N. W., 2012, *MNRAS*, 422, 207  
 Schuster W. J., Moreno E., Nissen P. E., Pichardo B., 2012, *A&A*, 538, A21  
 Sparke L. S., Casertano S., 1988, *MNRAS*, 234, 873  
 Toomre A., 1983, in *Internal Kinematics and Dynamics of Galaxies*, IAU Symposium 100, Athanassoula E., ed., pp. 177–185  
 Tremaine S., Frankel N., Bovy J., 2023, *MNRAS*, 521, 114  
 Vasiliev E., 2019, *MNRAS*, 482, 1525  
 Vasiliev E., Belokurov V., Erkal D., 2021, *MNRAS*, 501, 2279  
 Voskes T., Burton W. B., 1999, in *Astronomical Society of the Pacific Conference Series, Vol. 168, New Perspectives on the Interstellar Medium*, Taylor A. R., Landecker T. L., Joncas G., eds., p. 375  
 Weaver H., Williams D. R. W., 1974, *A&AS*, 17, 1  
 Weinberg M. D., 1989, *MNRAS*, 239, 549  
 Weinberg M. D., 1993, *ApJ*, 410, 543  
 Weinberg M. D., Blitz L., 2006, *ApJL*, 641, L33

## APPENDIX A: A SUBTLE POINT ABOUT EQUATION (5)

Here we discuss a delicate point that was skated over in the derivation of the equations of motion (13) in Section 2. The problem is made apparent by computing the potential  $\Phi_0(R)$  of the unperturbed axisymmetric disc. It is straightforward to show that equation (1) yields

$$\Phi_0(R) = -\frac{2G}{\sqrt{R}} \int dR' \sqrt{R' \Sigma(R')} Q_{-1/2}(\chi), \quad (\text{A1})$$

so the vertical acceleration of the disc is

$$\begin{aligned} a_{0z} &= -\frac{\partial \Phi_0}{\partial z} = \frac{2G}{\sqrt{R}} \int dR' \sqrt{R' \Sigma(R')} \frac{dQ_{-1/2}}{d\chi} \frac{z}{RR'}, \\ &= \frac{2Gz}{R^{3/2}} \int dR' \frac{\Sigma(R')}{\sqrt{R'}} \frac{dQ_{-1/2}}{d\chi}. \end{aligned} \quad (\text{A2})$$

As  $z \rightarrow 0$ , the acceleration tends to a finite value despite the factor  $z$  in front of the integral: the integral diverges as  $1/z$  because as  $z$  diminishes,  $\chi \rightarrow 1$  when  $R' = R$  and the derivative of  $Q$  diverges like  $1/(\chi - 1) \simeq 2(R/z)^2$ . This finding calls into question the legitimacy of pulling the derivative of  $Q$  out of the  $\phi'$  integral of equation (5).

By modelling the disc as razor-thin we have created a difficult situation. The vertical force changes sign at  $z = 0$  so it's not analytic there and cannot be Taylor expanded around  $z = 0$ . Physically, the vertical force at  $(R, \phi, z)$  is strongly dominated by material in the disc that lies within a circle of radius  $z$  about  $(R, \phi, 0)$ . Here the local component of the force on a star is effectively the force between a particle before and after displacement. We exclude this fictitious self-force by excluding  $R' = R$  from the integration over  $R'$ . That is, we break the integral into parts over  $(0, R - \epsilon_r)$  and  $(R + \epsilon_r, \infty)$  and let  $\epsilon_r$  become small without vanishing. With  $R' = R$  excluded,  $\chi$  remains greater than unity even if  $z - z'$  vanishes. Moreover, when  $|z - z'| \ll \epsilon_r$ ,  $Q$  and its derivatives become independent of  $z - z'$  and therefore independent of  $\phi'$ , so it's legitimate to pull  $dQ/d\chi$  out of the integral in equation (5).

Subtly different equations of motion are obtained in

HT69 by writing an expression for  $a_z$  directly (eq 2 in HT69) rather than obtaining  $a_z$  from the potential. Appendix B reproduces the derivation in HT69 using cylindrical rather than oblate-spheroidal coordinates. The integral of equation (B2) is stated to be the force from a sheet of dipoles with surface density proportional to  $h - h'$ . Actually the expression is only one of the two terms required for the force from a dipole. Appendix B makes a case that the other term can be neglected, but the case is delicate and HT69 does not attempt to make it.

In HT69 the contributions to  $a_z$  from  $h(R')$  and  $h(R)$  are separated. That proportional to  $h(R)$  is found to be associated with two discs with equal but opposite surface densities that are infinitesimally displaced in  $z$ , which is shown to be

$$a_{2z} = h(R, \phi) \frac{1}{R} \frac{\partial v_c^2}{\partial R}. \quad (\text{A3})$$

The other contribution is found by solving for the potential of a more complex sheet of dipoles using oblate spheroidal coordinates. An analogous solution using equations (1) yields the Fourier coefficients

$$\begin{aligned} a_{1m}(R) &= - \lim_{z \rightarrow 0} \frac{\partial \Phi_m}{\partial z} \\ &= - \frac{2G}{R^{3/2}} \int dR' \frac{D_m(R, R')}{\sqrt{R'}} \Sigma(R') h_m(R'), \end{aligned} \quad (\text{A4})$$

where

$$D_m(R, R') \equiv \lim_{z \rightarrow 0} \left( \frac{dQ_{|m|-1/2}}{d\chi} + \frac{z^2}{RR'} \frac{d^2 Q_{|m|-1/2}}{d\chi^2} \right) \Big|_{z'=0}. \quad (\text{A5})$$

Thus we encounter the same problem as before when  $R'$  passes through  $R$ , causing  $Q$  and its derivatives to diverge as  $z \rightarrow 0$ . By dividing the integral into parts of  $(0, R - \epsilon_r)$  and  $(R + \epsilon_r, \infty)$  we can argue that the second term in equation (A5) can be neglected because its contributions are more tightly confined around  $R = R'$  than those of the first term. Then equation (A4) yields essentially the first term in the integral of equation (10). HT69 does not regularise the integral over  $D_m$  as we have done in equation (10) by subtracting a term proportional to  $h(R, \phi)$ , so it arrives at equations that make sense only for a finite number of discrete rings.

Thus if extended to a continuum, the equations of motion in HT69 contain one divergent integral and a finite term. By contrast with the counter terms in equation (11) deleted we have two divergent integrals, and by inclusion of the counter terms both integrals are regularised. With the counter term deleted, equation (11) yields an integral for  $RN(R)$  that coincides with

$$\frac{2G}{\sqrt{R}} \int dR' \frac{D_0(R, R')}{\sqrt{R'}} \Sigma(R') \quad (\text{A6})$$

when the double derivative is dropped from the definition (A5) of  $D_0$ . Numerical evaluations show that the integral (A6) yields  $dv_c^2/dR$  only when the second derivative is included in  $D_0$  – the divergent contributions of the two terms in  $D_0$  cancel to produce the finite value that HT69 gives for the coefficient of  $h(R)$ . In our treatment the integral over  $dQ_{-1/2}/d\chi$  is regularised by an integral over  $dQ_{|m|-1/2}/d\chi$  rather than an integral over  $d^2 Q_{-1/2}/d\chi^2$  and the coefficient of  $h(R)$  in the equations of motion isn't  $(dv_c^2/dR)/R$ .

Decreasing the parameter  $\epsilon_z$  improves energy conservation at the cost of increased computational cost. In the computations below we have set  $\epsilon_r = 10^{-3}R$  and  $\epsilon_z = 10^{-4}R$ , where  $R$  is the radius at which the potential is required. With this choice the RMS variation in energy during the evolution shown in Fig. 2 is 2.5 per cent.

An appendix of Sparke & Casertano (1988) gives an insightful derivation of alternative expressions for vertical accelerations  $a_{1z}$  and  $a_{2z}$ . In these expressions  $a_{1z}$  and  $a_{2z}$  are obtained by integrating products of  $h_m$  and the kernel

$$B_m(R, R') \equiv \lim_{z \rightarrow 0} \int_0^\infty dk k^2 J_m(kR) J_m(kR') e^{-kz}, \quad (\text{A7})$$

where  $J_m$  is the usual cylindrical Bessel function. As  $z \rightarrow 0$  the integral over  $k$  becomes costly to evaluate on account of the oscillating nature of  $J_m$ . The Greens' function (1) provides an explicit formula for the analogous kernel, which moreover is not an oscillating function. Hence costly integrations are eliminated.

## APPENDIX B: VERTICAL FORCES ACCORDING TO HT69

We adapt the approach to computing vertical forces taken in HT69 to the use of the Greens' function (1). The gravitational acceleration at  $\mathbf{x}$  due to the mater at  $\mathbf{x}'$  is

$$d\mathbf{a}(\mathbf{x}) = \frac{G\Sigma(|\mathbf{x}'|)d^2\mathbf{x}'}{|\mathbf{x}' - \mathbf{x}|^3}(\mathbf{x}' - \mathbf{x}). \quad (\text{B1})$$

We are only interested in the vertical component of this acceleration. Since  $\mathbf{x}'$  lies above the point  $\mathbf{x}$  by  $h(\mathbf{x}') - h(\mathbf{x})$ , the vertical component is

$$da_z(\mathbf{x}, \mathbf{x}') = \frac{G\Sigma(|\mathbf{x}'|)d^2\mathbf{x}'}{|\mathbf{x}' - \mathbf{x}|^3}[h(\mathbf{x}') - h(\mathbf{x})]. \quad (\text{B2})$$

The gravitational acceleration  $\mathbf{a}(\mathbf{p}, \mathbf{x}, \mathbf{x}')$  at  $\mathbf{x}$  from a dipole  $\mathbf{p} = m\boldsymbol{\delta}$  at  $\mathbf{x}'$  is obtained by differencing the accelerations towards masses  $\pm m$  located at  $\mathbf{x}' \pm \frac{1}{2}\boldsymbol{\delta}$ .

$$\begin{aligned} \mathbf{a}(\mathbf{p}, \mathbf{x}, \mathbf{x}') &= G\mathbf{p} \cdot \frac{\partial}{\partial \mathbf{x}'} \frac{\mathbf{x}' - \mathbf{x}}{|\mathbf{x}' - \mathbf{x}|^3} \\ &= G \left( \frac{\mathbf{p}}{|\mathbf{x}' - \mathbf{x}|^3} - 3 \frac{\mathbf{p} \cdot (\mathbf{x}' - \mathbf{x})}{|\mathbf{x}' - \mathbf{x}|^5} (\mathbf{x}' - \mathbf{x}) \right) \end{aligned} \quad (\text{B3})$$

Now consider the difference in the accelerations produced by two distributions of dipoles over a disc. Let the dipoles be

$$\begin{aligned} d\mathbf{p}_1(\mathbf{x}') &= \Sigma(|\mathbf{x}'|)h(\mathbf{x}')d^2\mathbf{x}'\mathbf{e}_z \\ d\mathbf{p}_2(\mathbf{x}') &= \Sigma(|\mathbf{x}'|)h(\mathbf{x})d^2\mathbf{x}'\mathbf{e}_z. \end{aligned} \quad (\text{B4})$$

Then the difference in the accelerations they produce at  $\mathbf{x} = (R, h(\mathbf{x}), \phi)$  is

$$\begin{aligned} \mathbf{a}_1 - \mathbf{a}_2 &= G \int d^2\mathbf{x}' \Sigma(|\mathbf{x}'|) \left( \frac{h(\mathbf{x}') - h(\mathbf{x})}{|\mathbf{x}' - \mathbf{x}|^3} \mathbf{e}_z \right. \\ &\quad \left. - 3 \cos \theta \frac{|h(\mathbf{x}') - h(\mathbf{x})|}{|\mathbf{x}' - \mathbf{x}|^4} (\mathbf{x}' - \mathbf{x}) \right), \end{aligned} \quad (\text{B5})$$

where  $\theta$  is the angle between  $\mathbf{x}' - \mathbf{x}$  and  $\mathbf{e}_z$ . As  $h \rightarrow 0$ , the area of the disc within which this angle is not close to  $\pi/2$  shrinks, which suggests that in this limit the second term in the integrand can be neglected. A contrary consideration is

that this term grows faster than the other term by one power of  $|\mathbf{x} - \mathbf{x}'|^{-1}$  precisely where  $\cos\theta$  is non-negligible. HT69 implicitly assumes that the integral becomes dominated by the first term, which yields the required vertical acceleration (B2) and thus argue that the vertical acceleration produced by a warped disc can be obtained as the difference between the vertical accelerations produced by the dipole distributions (B4).

The acceleration  $a_{2z}$  can be evaluated from the unperturbed potential  $\Phi_0$  because it is just the acceleration due to two discs that differ only in the sign of  $\Sigma$  and are vertically separated by the constant  $h(\mathbf{x})$ . Hence

$$a_{2z}(\mathbf{x}) = h(\mathbf{x}) \frac{\partial^2 \Phi_0}{\partial z^2} \Big|_{\mathbf{x}}, \quad (\text{B6})$$

where  $z$  lies just above the disc. Here the density vanishes and Poisson's equation yields

$$\frac{\partial^2 \Phi_0}{\partial z^2} = -\frac{1}{R} \frac{\partial v_c^2}{\partial R}, \quad (\text{B7})$$

so<sup>3</sup>

$$a_{2z}(\mathbf{x}) = -\frac{h(\mathbf{x})}{R} \frac{\partial v_c^2}{\partial R}. \quad (\text{B8})$$

This acceleration depends on  $z$  only through  $h(\mathbf{x})$ , which is the amplitude of the dipole sheet; the acceleration above a given dipole sheet is independent of  $z$ .

We now compute the acceleration  $a_{1z}$  produced by the dipole distribution  $\mathbf{dp}_1$  in equation (B4). We expand the displacement field  $h(R, \phi)$  in the Fourier series (7) and use equation (1) to compute the contribution to  $a_{1z}$  from the dipole density  $p(R, \phi) = \Sigma(R)h_m(R)e^{im\phi}$ . Inserting the density  $\rho(R, z, \phi) = \sigma(R, \phi)\delta(z - \zeta)$  of a disc that lies in the plane  $z = \zeta$ , we obtain the Fourier coefficients

$$\Phi_m(R, z) \equiv -\frac{2G}{\sqrt{R}} \int dR' \sqrt{R'} \sigma_m(R') Q_{|m|-1/2}(\chi) \quad (\text{B9})$$

with  $\chi$  is evaluated with  $z' = \zeta$  and

$$\sigma_m(R') \equiv \int_0^{2\pi} \frac{d\phi'}{2\pi} \sigma(R', \phi') e^{im\phi'}. \quad (\text{B10})$$

The potential jointly generated by two razor-thin discs that carry opposite signs of mass and are separated by a small distance  $2\zeta$  has Fourier coefficients

$$\begin{aligned} \Phi_m(R, z) &= -\frac{2G}{\sqrt{R}} \int dR' \sqrt{R'} \sigma_m(R') [Q_{|m|-1/2}(\chi(z' = \zeta)) \\ &\quad - Q_{|m|-1/2}(\chi(z' = -\zeta))] \\ &= \frac{2G}{\sqrt{R}} \int dR' \sqrt{R'} p_m(R') \frac{dQ_{|m|-1/2}}{d\chi} \Big|_{z'=0} \frac{z}{RR'}, \end{aligned} \quad (\text{B11})$$

where  $p_m(R) = 2\zeta\sigma_m(R)$  is the Fourier component of the dipole density represented by the two sheets.  $Q_{|m|-1/2}(\chi)$  diverges like  $\ln(\chi - 1)$  as  $\chi \rightarrow 1$ . Consequently, as  $\chi \rightarrow 1$  the derivative in equation (B11) diverges like  $1/(\chi - 1)$  so

<sup>3</sup> Notice that  $a_{2z}/h$  is negative near the centre where  $v_c$  is rising. The integral over the first term in our expression (B3) for a dipole's acceleration inevitably makes a positive contribution to  $a_z/h$ , so the negativity of  $a_{2z}/h$  is caused by the second term in (B3), which does not appear in HT69.

as  $R \rightarrow R'$  and  $z \rightarrow 0$  the product of  $z$  and the derivative of  $Q$  diverges. Nonetheless, the integral over  $R'$  at nonzero  $z$  tends to a finite limit as  $z \rightarrow 0$ . The limit's value is the potential just above the dipole sheet. The potential below the sheet is minus that value.

To obtain the vertical accelerations that we need, we set  $p_m(R') = \Sigma(R')h_m(R')$  in equation (B11) and compute

$$\begin{aligned} a_m(R') &= -\lim_{z \rightarrow 0} \frac{\partial \Phi_m}{\partial z} \\ &= -\frac{2G}{R^{3/2}} \int dR' \frac{D(R')}{\sqrt{R'}} \Sigma(R') h_m(R'), \end{aligned} \quad (\text{B12})$$

where

$$D(R, R') \equiv \lim_{z \rightarrow 0} \frac{\partial}{\partial z} \left( z \frac{dQ_{|m|-1/2}}{d\chi} \right) \Big|_{z'=0}. \quad (\text{B13})$$

### APPENDIX C: ENERGY INTEGRALS

With  $h(R, \phi, t)$  the distance of the disc above the plane  $z = 0$ , the equation of motion of a star is

$$\frac{\partial^2 h}{\partial t^2} + 2\Omega(R) \frac{\partial^2 h}{\partial t \partial \phi} + \Omega^2 \frac{\partial^2 h}{\partial \phi^2} = G \int d^2 \mathbf{R}' \Sigma(R') \frac{h(\mathbf{R}') - h(\mathbf{R})}{|\mathbf{R} - \mathbf{R}'|^3}. \quad (\text{C1})$$

We multiply by  $\Sigma(R)(\partial h/\partial t)d^2 \mathbf{R}$  and integrate

$$\begin{aligned} \int d^2 \mathbf{R} \Sigma \left( \frac{\partial^2 h}{\partial t^2} \frac{\partial h}{\partial t} + 2\Omega \frac{\partial^2 h}{\partial t \partial \phi} \frac{\partial h}{\partial t} + \Omega^2 \frac{\partial^2 h}{\partial \phi^2} \frac{\partial h}{\partial t} \right) &= G \int d^2 \mathbf{R} \\ &\times \int d^2 \mathbf{R}' \Sigma(R) \Sigma(R') \frac{h(\mathbf{R}') - h(\mathbf{R})}{|\mathbf{R} - \mathbf{R}'|^3} \frac{\partial h(\mathbf{R})}{\partial t}. \end{aligned} \quad (\text{C2})$$

The middle term on the left can be rearranged to

$$\Omega(R) \frac{\partial}{\partial \phi} \left( \frac{\partial h}{\partial t} \right)^2, \quad (\text{C3})$$

which vanishes when integrated over  $\phi$ . After using  $(\partial^2 h/\partial \phi^2) = -m^2 h$ , the derivative w.r.t.  $t$  can be taken out of the remaining integral. The right side of equation (C2) only changes its sign when the primed and unprimed variables are swapped. So we can subtract its swapped version and halve the result, to obtain

$$\begin{aligned} 0 &= \frac{d}{dt} \left\{ \frac{1}{2} \int d^2 \mathbf{R} \Sigma \left( \left( \frac{\partial h}{\partial t} \right)^2 - m^2 \Omega^2 h^2 \right) \right. \\ &\quad \left. + \frac{G}{4} \int d^2 \mathbf{R} \int d^2 \mathbf{R}' \Sigma(R) \Sigma(R') \frac{[h(\mathbf{R}') - h(\mathbf{R})]^2}{|\mathbf{R} - \mathbf{R}'|^3} \right\} \end{aligned} \quad (\text{C4})$$

which gives us an energy integral for each  $m$ .

When  $m = 0$ , this integral provides a proof of stability because then the potential energy comprises the manifestly non-negative double integral. When  $m \neq 0$  the single integral contains a negative contribution to the potential energy and stability is not evident. For the case  $m = 1$  Hunter & Toomre were able to demonstrate stability by combining the potential energy terms into a single non-negative double integral as follows.

Poisson's integral for the potential of the unperturbed disc is

$$\Phi(R) = - \int d^2 \mathbf{R}' \frac{G \Sigma(R')}{\sqrt{R^2 + R'^2 - 2RR' \cos(\phi' - \phi)}}. \quad (\text{C5})$$

Differentiating we get

$$\Omega^2(R) = \frac{1}{R} \frac{\partial \Phi}{\partial R} = G \int d^2 \mathbf{R}' \Sigma(R') \frac{1 - (R'/R) \cos(\phi' - \phi)}{|\mathbf{R} - \mathbf{R}'|^3}. \quad (\text{C6})$$

Inserting this into equation (C2) with  $m = 1$ , we find

$$\begin{aligned} \frac{d}{dt} \frac{1}{2} \int d^2 \mathbf{R} \Sigma \left( \frac{\partial h}{\partial t} \right)^2 &= G \int d^2 \mathbf{R} \int d^2 \mathbf{R}' \Sigma(R) \Sigma(R') \\ &\times \frac{h(\mathbf{R}') - h(\mathbf{R})(R'/R) \cos(\phi' - \phi)}{|\mathbf{R} - \mathbf{R}'|^3} \frac{\partial h(\mathbf{R})}{\partial t}. \end{aligned} \quad (\text{C7})$$

In the double integral over angles on the right we change the inner integration variable from  $\phi'$  to  $\Delta \equiv \phi' - \phi$ , which already occurs in both the numerator and denominator. Now

$$\begin{aligned} h(\mathbf{R}') &= h(R', \phi') = h(R', \phi + \Delta) \\ &= h_c \cos(\phi + \Delta) + h_s \sin(\phi + \Delta) \\ &= h_c [\cos \phi \cos \Delta - \sin \phi \sin \Delta] + h_s [\sin \phi \cos \Delta + \cos \phi \sin \Delta] \\ &= [h_c \cos \phi + h_s \sin \phi] \cos \Delta + [-h_c \sin \phi + h_s \cos \phi] \sin \Delta \\ &= h(R', \phi) \cos \Delta + h(R', \phi + \pi/2) \sin \Delta. \end{aligned} \quad (\text{C8})$$

When we replace  $h(\mathbf{R}')$  in the numerator of equation (C7) with this expression, the term proportional to  $\sin \Delta$  vanishes on integration over  $\Delta$  because it's an odd function of  $\Delta$  while the denominator is an even function so the integrand is odd. After the replacement we therefore have

$$\begin{aligned} \frac{d}{dt} \frac{1}{2} \int d^2 \mathbf{R} \Sigma \left( \frac{\partial h}{\partial t} \right)^2 &= G \int dR R \Sigma(R) \int dR' R' \Sigma(R') \\ &\times \int d\phi [h(R', \phi) - h(R, \phi)(R'/R)] \frac{\partial h(\mathbf{R})}{\partial t} \int_0^{2\pi} d\Delta \frac{\cos \Delta}{|\mathbf{R} - \mathbf{R}'|^3} \\ &= -\frac{G}{4} \frac{d}{dt} \int dR \Sigma(R) \int dR' \Sigma(R') \\ &\times \int d\phi [Rh(R', \phi) - R'h(R, \phi)]^2 \int_0^{2\pi} d\Delta \frac{\cos \Delta}{|\mathbf{R} - \mathbf{R}'|^3}. \end{aligned} \quad (\text{C9})$$

The argument of the time derivative on the right is now manifestly non-negative, which establishes stability except when the argument is identically zero, which it is when  $Rh(R', \phi) = R'h(R, \phi)$ . This condition is satisfied when the perturbation amounts to a tilt of the whole disc about an axis that lies in the plane – it's physically obvious that such tilts should involve no potential energy and thus be neutrally stable.

The integral over  $\Delta$  in equation (C9) simplifies:

$$\begin{aligned} \int d\Delta \frac{\cos \Delta}{|\mathbf{R} - \mathbf{R}'|^3} &= \int d\Delta \frac{\cos \Delta}{[R^2 + R'^2 - 2RR' \cos \Delta]^{3/2}} \\ &= \frac{g(\chi)}{[R^2 + R'^2]^{3/2}}, \end{aligned} \quad (\text{C10})$$

where  $\chi$  is defined by equation (2) and

$$g(\chi) \equiv 2 \int_0^\pi d\Delta \frac{\cos \Delta}{(1 - \chi^{-1} \cos \Delta)^{3/2}}. \quad (\text{C11})$$

The integral over  $\phi$  in equation (C9) can be executed analytically. We use that  $h(\phi) = 2(h_r \cos \phi - h_i \sin \phi)$ , where  $h_r$

and  $h_i$  are the real and imaginary parts of  $h$ . Then

$$\begin{aligned} \frac{1}{4} \int d\phi [Rh(R', \phi) - R'h(R, \phi)]^2 \\ &= \int d\phi \left\{ R[h_r(R') \cos \phi - h_i(R') \sin \phi] \right. \\ &\quad \left. - R'[h_r(R) \cos \phi - h_i(R) \sin \phi] \right\}^2 \\ &= \pi [Rh_r(R') - R'h_r(R)]^2 + \pi [Rh_i(R') - R'h_i(R)]^2. \end{aligned} \quad (\text{C12})$$

With these results, equation (C9) becomes the statement that for  $m = 1$  the conserved energy is

$$\begin{aligned} E &= 2\pi \int dR R \Sigma(R) \left[ \left( \frac{\partial h_r}{\partial t} \right)^2 \right. \\ &\quad \left. + \left( \frac{\partial h_i}{\partial t} \right)^2 \right] + \pi G \int dR \Sigma(R) \int dR' \frac{\Sigma(R') g(\chi)}{[R^2 + R'^2]^{3/2}} \\ &\times \left\{ [Rh_r(R') - R'h_r(R)]^2 + [Rh_i(R') - R'h_i(R)]^2 \right\}. \end{aligned} \quad (\text{C13})$$

The double integral is symmetric in  $R, R'$  so is equal to twice the integral over  $R' < R$ . In terms of  $s \equiv \ln(R'/R)$  we have

$$\begin{aligned} PE &= 2\pi G \int_0^\infty dR \Sigma(R) \int_{-\infty}^0 ds \Sigma(R') \frac{e^s g(\chi)}{[1 + e^{2s}]^{3/2}} \\ &\times \left\{ [h_r(R') - e^s h_r(R)]^2 + [h_i(R') - e^s h_i(R)]^2 \right\}. \end{aligned} \quad (\text{C14})$$

As  $R \rightarrow R'$ ,  $g(\chi)$  diverges but the integrand remains finite because the curly bracket then tends to zero.